Research Article Vol. 29, No. 1 / 4 January 2021 / Optics Express 256
Optics EXPRESS

Mid-infrared spectrally-uncorrelated biphotons generation from doped PPLN: a theoretical investigation

BEI WEI,[1,6] WU-HAO CAI,[1,6] CHUNLING DING,[1] GUANG-WEI DENG,[2,3,7] RYOSUKE SHIMIZU,[4] QIANG ZHOU,[2,3,8] AND RUI-BO JIN[1,5,9]

[1]*Hubei Key Laboratory of Optical Information and Pattern Recognition, Wuhan Institute of Technology, Wuhan 430205, China*
[2]*Institute of Fundamental and Frontier Sciences and School of Optoelectronic Science and Engineering, University of Electronic Science and Technology of China, Chengdu 610054, China*
[3]*CAS Key Laboratory of Quantum Information, University of Science and Technology of China, Hefei 230026, China*
[4]*The University of Electro-Communications, 1-5-1 Chofugaoka, Chofu, Tokyo, Japan*
[5]*State Key Laboratory of Quantum Optics and Quantum Optics Devices, Shanxi University, Taiyuan, 030006, China*
[6]*These authors contributed equally to this work*
[7]*gwdeng@uestc.edu.cn*
[8]*zhouqiang@uestc.edu.cn*
[9]*jrbqyj@gmail.com*

Abstract: We theoretically investigate the preparation of mid-infrared (MIR) spectrally-uncorrelated biphotons from a spontaneous parametric down-conversion process using doped LN crystals, including MgO doped LN, ZnO doped LN, and In_2O_3 doped ZnLN with doping ratio from 0 to 7 mol%. The tilt angle of the phase-matching function and the corresponding poling period are calculated under type-II, type-I, and type-0 phase-matching conditions. We also calculate the thermal properties of the doped LN crystals and their performance in Hong-Ou-Mandel interference. It is found that the doping ratio has a substantial impact on the group-velocity-matching (GVM) wavelengths. Especially, the GVM_2 wavelength of co-doped InZnLN crystal has a tunable range of 678.7 nm, which is much broader than the tunable range of less than 100 nm achieved by the conventional method of adjusting the temperature. It can be concluded that the doping ratio can be utilized as a degree of freedom to manipulate the biphoton state. The spectrally uncorrelated biphotons can be used to prepare pure single-photon source and entangled photon source, which may have promising applications for quantum-enhanced sensing, imaging, and communications at the MIR range.

1. Introduction

The mid-infrared (MIR) wavelength range (approximately 2-20 μm) is of great interest to a variety of scientific and technological applications in sensing, imaging, and communications [1,2]. Firstly, this range contains strong absorption bands of a variety of gases, leads to essential applications in gas sensing [3] and environmental monitoring [4]. Secondly, the MIR region covers the atmospheric transmission window between 3 μm and 5 μm. This region with relatively high transparency is beneficial for atmospheric monitoring and free-space communications [5]. Thirdly, room temperature objects emit light at MIR wavelengths, resulting in novel applications in infrared thermal imaging [6,7]. Fourthly, with the rapid development of optical fiber communications, there is a growing demand to expand the communication wavelengths into the MIR region to increase the communication bandwidth [8].

#412603 https://doi.org/10.1364/OE.412603
Journal © 2021 Received 14 Oct 2020; revised 25 Nov 2020; accepted 11 Dec 2020; published 22 Dec 2020

Optics EXPRESS

All these practical applications mentioned above are based on strong light sources in the MIR region. However, the advantages of the MIR range have not been fully exploited using quantum technology. In order to further improve the sensitivity in those applications, one promising approach is to utilize a single-photon source or entangled photon source in the MIR region. Spontaneous parametric down-conversion (SPDC) is one of the widely used methods to prepare biphotons, which can be used to produce single-photon source and entangled photon source. Previously, several theoretical and experimental works have been dedicated to the development of single or entangled photon source in MIR range from an SPDC process. In 2016, Lee et al. calculated the extended phase-matching properties of periodically poled potassium niobate (PPKN) for single-photon generation at the MIR range [9]. In 2017, Mancinelli et al. performed coincidence measurements on twin photons generated from periodically poled lithium niobate (PPLN) at 3.1 μm [7]. In 2018, McCracken et al. numerically investigated the mid-infrared single-photon generation in a range of novel nonlinear materials, including PPLN, PPKTP, GaP, GaAs, $CdSiP_2$, and $ZnGeP_2$ [10]. In 2019, Rosenfeld et al. experimentally prepared MIR photon pairs in a four-wave mixing process from a silicon-on-insulator waveguide at around 2.1 μm [11]. In 2020, Kundys et al. numerically studied the reconfigurable MIR single-photon sources based on functional ferroelectrics, i.e., PMN-0.38PT crystal at 5.6 μm [12]. In the same year, Prabhakar et al. experimentally demonstrated the entangled photons generation and Hong-Ou-Mandel interference at 2.1 μm from PPLN crystals [13].

Many biphoton sources have been demonstrated in the previous studies [7,9,10,12,13]; however, from the experimental point of view, it is still lack of high-quality biphotons source at the MIR range, especially the spectrally uncorrelated biphotons [14–18]. The biphotons generated from an SPDC process are generally spectrally correlated due to the energy and momentum conservation laws. However, it is necessary to utilize biphotons with no spectral correlations to obtain the heralded pure-state single photon for many quantum information processing (QIP) protocols, such as quantum computation [19], boson sampling [20], quantum teleportation [21], and measurement-device-independent quantum key distribution [22]. In quantum sensing, a high-NOON state, which provides high accuracy for phase-sensitive measurements, should be prepared from spectrally uncorrelated biphotons [23,24]. Therefore, spectrally uncorrelation of photon pairs from SPDC is indispensable for the future development of quantum information at the MIR range.

In this work, we investigate the generation of spectrally uncorrelated biphotons from PPLN crystals at MIR range. PPLN has the merits of large nonlinear coefficient and wide transparency range (0.4 $\sim$ 5 μm) [25–28]. Another unique advantage of PPLN is that its intrinsical group-velocity-matched (GVM) wavelengths are in the MIR range, and the spectrally uncorrelated biphoton state can be engineered at the GVM wavelengths [14,29].

In addition, we also consider the manipulation of the biphoton state by adding different dopants in PPLN. Traditionally, PPLN is doped with different dopants to improve its properties. For example, by doping Mg and Zr, the damage resistance can be improved from visible to ultraviolet region [30]; by doping Zn, the electro-optical coefficients can be improved [31]; by doping Fe, the photorefractive properties can be improved [32]. Especially, doping rare-earth elements (e.g., Tm, Er, Dy, Tb, Gd, Pr) makes PPLN a right candidate for lasers and quantum memories [33,34]. It is natural to deduce that doping can also be utilized as a degree of freedom to manipulate the single photons state at the MIR range. Therefore, we study the spectrally uncorrelated biphotons generation from doped PPLN in this work. Specifically, we investigated the GVM wavelengths, the tilt angle, the poling period, the thermal properties, and the HOM interferences of biphtons generated from three kinds of doped LN crystals, including MgLN [MgO(x mol%)$LiNbO_3$], ZnLN [ZnO(x mol%)$LiNbO_3$], and InZnLN [In_2O_3(x mol%)ZnO(5.5 mol%)$LiNbO_3$, with x from 0 to 7].

Optics EXPRESS

2. Theory

The biphoton state $|\psi\rangle$ generated from SPDC can be expressed as [35]

$$|\psi\rangle = \int_0^\infty \int_0^\infty \mathrm{d}\omega_s \, \mathrm{d}\omega_i f(\omega_s, \omega_i)\hat{a}_s^\dagger(\omega_s)\hat{a}_i^\dagger(\omega_i)|0\rangle|0\rangle, \tag{1}$$

where ω is the angular frequency, $\hat{a}^\dagger$ is the creation operator, and the subscripts s and i indicate the signal and idler photon. The joint spectral amplitude (JSA) $f(\omega_s, \omega_i)$ can be calculated as the product of the pump envelope function (PEF) $\alpha(\omega_s, \omega_i)$ and the phase-matching function (PMF) $\phi(\omega_s, \omega_i)$:

$$f(\omega_s, \omega_i) = \alpha(\omega_s, \omega_i) \times \phi(\omega_s, \omega_i). \tag{2}$$

A PEF with a Gaussian-distribution can be written as

$$\alpha(\omega_s, \omega_i) = \exp[-\frac{1}{2}\left(\frac{\omega_s + \omega_i - \omega_{p_0}}{\sigma_p}\right)^2], \tag{3}$$

where ω_{p_0} is the center angular frequency of the pump; σ_p is the bandwidth of the pump, and the subscript p indicates the pump photon. The full-width at half-maximum (FWHM) is $\mathrm{FWHM}_\omega = 2\sqrt{\ln(2)}\sigma_p \approx 1.67\sigma_p$.

If we choose wavelengths as the variables, the PEF can be rewritten as

$$\alpha(\lambda_s, \lambda_i) = \exp\left(-\frac{1}{2}\left\{\frac{1/\lambda_s + 1/\lambda_i - 1/(\lambda_0/2)}{\Delta\lambda/[(\lambda_0/2)^2 - (\Delta\lambda/2)^2]}\right\}^2\right), \tag{4}$$

where $\lambda_0/2$ is the central wavelength of the pump; The FWHM of the pump at intensity level is $\mathrm{FWHM}_\lambda = \frac{2\sqrt{\ln(2)}\lambda_0{}^2\Delta\lambda(\lambda_0{}^2-\Delta\lambda^2)}{\lambda_0{}^4+\Delta\lambda^4-2\lambda_0{}^2\Delta\lambda^2[1+\ln(4)]}$. For $\Delta\lambda << \lambda_0$, $\mathrm{FWHM}_\lambda \approx 2\sqrt{\ln(2)}\Delta\lambda \approx 1.67\Delta\lambda$.

The PMF function can be written as

$$\phi(\omega_s, \omega_i) = \mathrm{Sinc}\left(\frac{\Delta kL}{2}\right), \tag{5}$$

where L is the length of the crystal, $\Delta k = k_p - k_i - k_s \pm \frac{2\pi}{\Lambda}$ and $k = \frac{2\pi n(\lambda)}{\lambda}$ is the wave vector. Λ is the poling period and can be calculated by

$$\Lambda = \frac{2\pi}{|k_p - k_i - k_s|}. \tag{6}$$

The angle θ between the ridge direction of PMF and the horizontal axis is determined by [36]

$$\tan\theta = -\left(\frac{V_{g,p}^{-1}(\omega_p) - V_{g,s}^{-1}(\omega_s)}{V_{g,p}^{-1}(\omega_p) - V_{g,i}^{-1}(\omega_i)}\right), \tag{7}$$

where $V_{g,\mu} = \frac{d\omega}{dk_\mu(\omega)} = \frac{1}{k'_\mu(\omega)}, (\mu = p, s, i)$ is the group velocity. The shape of the JSA is determined by the following three GVM conditions [37,38].

Optics EXPRESS

The GVM_1 condition ($\theta = 0°$):

$$V_{g,p}^{-1}(\omega_p) = V_{g,s}^{-1}(\omega_s). \tag{8}$$

The GVM_2 condition ($\theta = 90°$):

$$V_{g,p}^{-1}(\omega_p) = V_{g,i}^{-1}(\omega_i). \tag{9}$$

The GVM_3 condition ($\theta = 45°$):

$$2V_{g,p}^{-1}(\omega_p) = V_{g,s}^{-1}(\omega_s) + V_{g,i}^{-1}(\omega_i). \tag{10}$$

The purity can be calculated by performing Schmidt decomposition on $f(\omega_s, \omega_i)$:

$$f(\omega_s, \omega_i) = \sum_j c_j \phi_j(\omega_s)\varphi_j(\omega_i), \tag{11}$$

where $\phi_j(\omega_s)$ and $\varphi_j(\omega_i)$ are the two orthogonal basis vectors in the frequency domain, and c_j is a set of non-negative real numbers that satisfy the normalization condition $\sum_j c_j^2 = 1$. The purity p is defined as:

$$p = \sum_j c_j^4. \tag{12}$$

GVM wavelengths are important parameters for nonlinear crystals. The maximal purities under GVM_1, GVM_2, and GVM_3 conditions are around 0.97, 0.97, and 0.82, respectively [37].

Note the three GVM conditions in Eqs. (8–10) are also called fully-asymmetric GVM or symmetric GVM conditions in Ref. [17]. In fact, the spectrally-pure state can be prepared for any θ angle between 0 and 90 degrees, independently from the PDC-type (type-0, type-I, or type-II) and wavelength degeneracy (degenerated or non-degenerated). Perfectly separable JSA can be achieved only with Gaussian pump and Gaussian PMF (via domain engineering techniques), as proven in Ref. [39]. However, the three GVM conditions listed in Eqs. (8–10) with the degenerated wavelengths are the most widely used cases in the experiments [40–42]. Especially, the GVM_3 condition has a symmetric distribution along the anti-diagonal direction, i.e., $f(\omega_s, \omega_i) = f(\omega_i, \omega_s)$, which is the prerequisite condition for high-visibility HOM interferences. Therefore, we mainly focus on the type-II phase-matching condition in the calculation below.

3. Calculation and simulation

In this section, we first calculate the angle θ in the range of 0 and 90 degrees, and the corresponding poling period Λ under type-II, type-I, and type-0 phase-matching conditions. Then, we consider the thermal properties, and the HOM interferences for the doped PPLN crystals under the type-II phase-matching condition. The Sellmeier equations for these crystals are chosen from Refs. [43–45], where the Sellmeier equations are parameterized by the dopant concentration. The PPLN crystals are negative uniaxial crystals ($n_o > n_e$), where $n_{o(e)}$ is the refractive index of the ordinary (extraordinary) ray.

3.1. Angle θ and poling period Λ for type-II phase-matching condition

In the calculation below, we consider type-II phase-matched ($o \rightarrow o + e$) SPDC in a collinear configuration with wavelength degenerated ($2\lambda_p = \lambda_s = \lambda_i$) or non-degenerated ($\lambda_s \neq \lambda_i$). In the type-II phase-matching condition, we set the pump and the signal as o-ray, and the idler as e-ray. Figure 1(a-c) shows the tilt angle θ as a function of the doping ratio (x mol %) and signal/idler (degenerated) wavelength. For MgLN in Fig. 1(a), on the line of $\theta = 0°$, the GVM_1 wavelength increased monotonically, i.e., from 2478.6 nm at $x = 0$ to 2472.7 nm at $x = 7$. For $\theta = 90°$, the GVM_2 wavelength increased non-monotonically from 3931.4 nm ($x = 0$) to the maximal

Optics EXPRESS

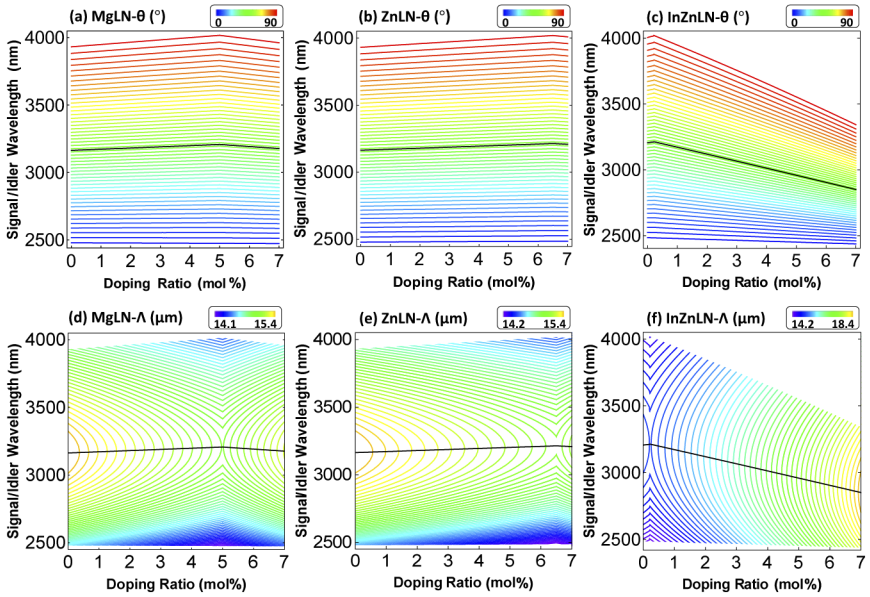

Fig. 1. (a-c): The tilt angle θ as a function of signal (idler) wavelength and doping ratio x for MgLN [MgO(x mol%):LiNbO3], ZnLN [ZnO(x mol%):$LiNbO_3$], and InZnLN [In_2O_3(x mol%):ZnO(5.5 mol%):$LiNbO_3$]. (d-f): The corresponding poling period. In these figures, the signal and the idler photons have degenerated wavelengths under the **type-II** phase-matching condition. The solid black line indicates $\theta = 45°$.

value of 4016.6 nm ($x = 5$), and then decreased to 3961.6 nm ($x = 7$). For $\theta = 45°$, the GVM_3 wavelength also increased non-monotonically, i.e., increased from 3163.6 nm ($x = 0$) to 3207.6 nm ($x = 5$), and then decreased to 3177.1 nm ($x = 7$).

For ZnLN in Fig. 1(b), on the line of $\theta = 0°$, the GVM_1 wavelength increased monotonically from 2478.6 nm at $x = 0$ to 2485.8 nm at $x = 7$. On the line of $\theta = 90°$, the GVM_2 wavelength started from 3931.4 nm at $x = 0$, and reached a maximal value of 4019.3 nm at $x = 6.5$, and then decreased to 4009.0 nm at $x = 7$. On the line of $\theta = 45°$, the GVM_3 wavelength is 3163.6 nm, 3213.6 nm, and 3208.2 nm, at $x = 0$, 6.5, and 7, respectively.

For InZnLN in Fig. 1(c), the GVM_1 ($\theta = 0°$) wavelength decreased monotonically from 2484.3 nm at $x = 0$ to 2436.9 nm at $x = 7$. The GVM_2 ($\theta = 90°$) wavelength increased non-monotonically: started from 4006.0 nm at $x = 0$ and reached a maximal value of 4021.6 nm at $x = 0.2$, and then decreased to 3342.9 nm at $x = 7$. The GVM_3 ($\theta = 45°$) wavelength also increased non-monotonically, the wavelengths are 3205.9 nm, 3213.9 nm, and 2850.4 nm at $x = 0$, 0.2, and 7, respectively. Figure 1(d-f) shows the poling period for each crystal. Λ is 14.1 μm to 15.4 μm for MgLN, 14.2 μm to 15.4 μm for ZnLN, and 14.2 μm to 18.4 μm for InZnLN. For comparison, we also list the wavelength of GVM_1, GVM_2, and GVM_3 at different doping ratios in Table 1. It can be discovered in Table 1 that the co-doped crystal, InZnLN, has a large tunable wavelength range of 678.7 nm. This feature is essential for quantum state engineering at the MIR wavelength range.

Next, we consider the wavelength non-degenerated cases for a fixed doping ratio, i.e., MgO(5 mol%):LiNbO3, ZnO(5 mol%): $LiNbO_3$, and In_2O_3(5 mol%): ZnO(5.5 mol%): $LiNbO_3$.

Figure 2(a-c) shows the angle θ as a function of the pump and the signal wavelengths for MgLN, ZnLN, InZnLN, with the same doping ratio of 5 mol%. On the line of $\theta = 0°$ ($\theta = 90°$), the signal wavelength decreases (increases) monotonically with the increase of the pump wavelength.

Optics EXPRESS

Table 1. Summary of the GVM wavelengths in Fig. 1 at different doping ratios. The maximal λ_{GVM} is achieved at the doping ratio of 5 mol% for MgLN, 6.5 mol% for ZnLN, and 0.2 mol% for InZnLN. $\Delta\lambda$ is the maximal difference of the GVM wavelengths.

Crystal Name	MgLN	ZnLN	InZnLN
λ_{GVM1} at 0 mol% (nm)	2478.6	2478.6	2484.3
λ_{GVM1} at 7 mol% (nm)	2472.7	2485.8	2436.9
$\Delta\lambda_{GVM1}$ (nm)	5.9	-7.2	47.4
λ_{GVM2} at 0 mol% (nm)	3931.4	3931.4	4006.0
λ_{GVM2} at 7 mol% (nm)	3961.6	4009.0	3342.9
Maximum of λ_{GVM2}	4016.6	4019.3	4021.6
$\Delta\lambda_{GVM2}$ (nm)	-85.2	-87.9	678.7
λ_{GVM3} at 0 mol% (nm)	3163.6	3163.6	3205.9
λ_{GVM3} at 7 mol% (nm)	3177.1	3208.2	2850.4
Maximum of λ_{GVM3}	3207.6	3213.6	3213.9
$\Delta\lambda_{GVM3}$ (nm)	-44.0	-50.0	363.5

On the line of $\theta = 45°$, the signal wavelength changes non-monotonically. Figure 2(d-f) shows the corresponding poling period Λ, ranging from 5.0 μm to 18.0 μm for the three crystals.

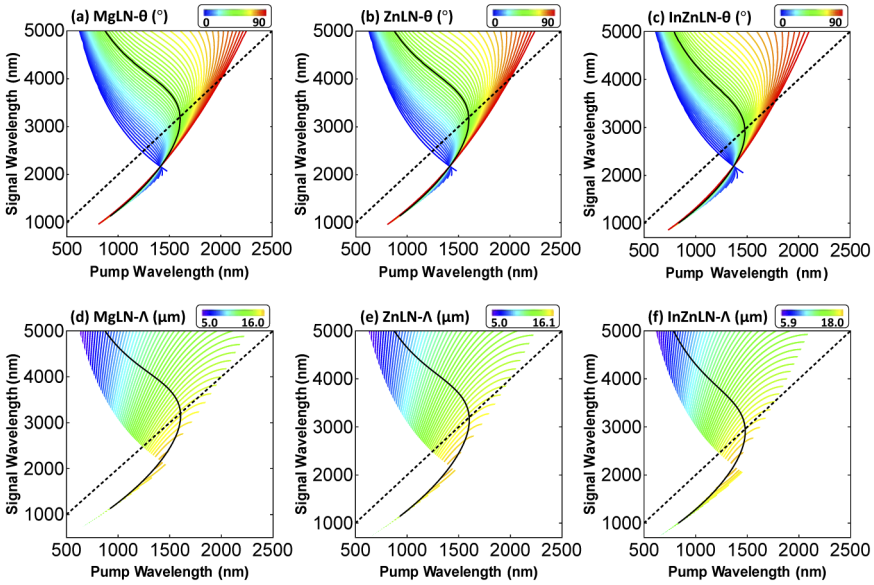

Fig. 2. (a-c): The tilt angle θ as functions of the signal wavelength and the pump wavelength for crystals with fixed doping ratio, i.e., MgLN [MgO(5 mol%):LiNbO3], ZnLN [ZnO(5 mol%):$LiNbO_3$], and InZnLN [In_2O_3(5 mol%):ZnO(5.5 mol%):$LiNbO_3$]. (d-f): The corresponding poling period. In these figures, the signal and the idler photons have the non-degenerated wavelengths under the **type-II** phase-matching condition. The solid black line indicates $\theta = 45°$, and the dashed black line indicates $\lambda_s = 2\lambda_p$.

3.2. Angle θ and poling period Λ for type-I and type-0 phase-matching conditions

It is also possible to prepare spectrally pure states under the type I and type-0 phase-matching conditions, as long as the angle θ is between 0° and 90°. Type-0 and type-I PDC in PPLN

Optics EXPRESS

are routinely used in many quantum optics experiments, e.g., in biphoton states generation and frequency conversion [46,47]. Figure 3(a-c) shows the angle θ as a function of the pump and the signal wavelengths under type-I ($e \rightarrow o + o$) phase-matching condition. The pump wavelength is in the range of 300-900 nm and the signal is in the range of 500-5000 nm. Figure 3(d-f) shows the corresponding poling period Λ, ranging from 9.3 μm to 79.0 μm. For wavelengths near the degenerated case, the poling period is larger than the case of far from the degenerated condition. The Λ of InZnLN is larger than the values of MgLN and ZnLN.

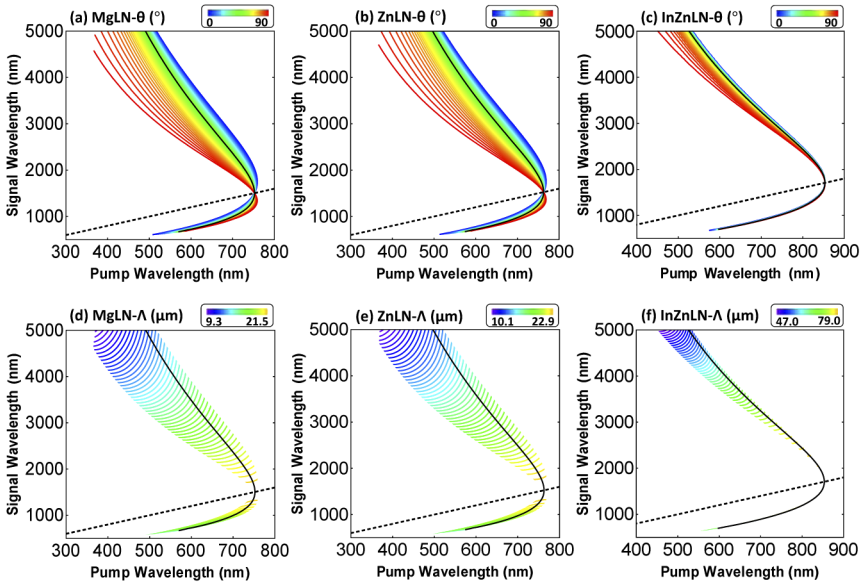

Fig. 3. (a-c): The tilt angle θ as a function of the signal wavelength and the pump wavelength for crystals with fixed doping ratio, i.e., MgLN [MgO(5 mol%):LiNbO3], ZnLN [ZnO(5 mol%):$LiNbO_3$], and InZnLN [In_2O_3(5 mol%):ZnO(5.5 mol%):$LiNbO_3$]. (d-f): The corresponding poling period. In these figures, the signal and the idler photons have the non-degenerated wavelengths under **type-I** phase-matching condition. The solid black line indicates $\theta = 45°$, and the dashed black line indicates $\lambda_s = 2\lambda_p$.

Figure 4(a-c) shows the case for type-0 ($e \rightarrow e + e$) phase-matching condition. The pump wavelength is in the range of 600-1500 nm, and the signal is in the range of 700-5000 nm. The corresponding poling period Λ is between 13.6 μm to 27.7 μm, as shown in Fig. 4(d-f). The three crystals have a similar performance under the type-0 phase matching-condition.

3.3. Thermal properties

In this subsection, we investigate the thermal properties of the doped PPLN crystals. Temperature is a crucial parameter for quasi-phase-matched (QPM) crystals, since the phase-matching conditions in the QPM crystals are mainly controlled by temperature in the experiments. Using the temperature-dependent Sellmeier equations in Refs. [43–45], we can calculate the GVM wavelength as a function of the temperature. We first consider the case of MgLN with different doping ratios, and then we compare MgLN with ZnLN and InZnLN at a fixed doping ratio. Figure 5(a) shows the case of GVM_1 wavelength, which increases linearly with the increase of temperature. When the temperature increases from $20°C$ to $120°C$, the GVM wavelength increases by about 2.8 nm for all the doping ratio from 0 to 7 mol%. Figure 5(b) and (c) show the cases of GVM_2 and GVM_3 wavelengths, which decrease by about 78 nm and 40 nm respectively when the temperature increases from $20°C$ to $120°C$. By comparing Figs. 5(a), (b), and (c), it can

Optics EXPRESS

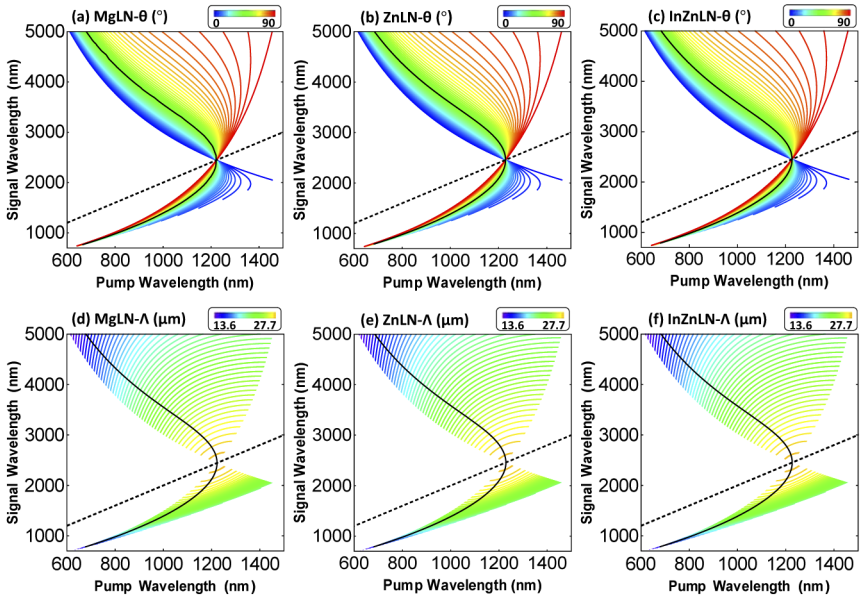

Fig. 4. (a-c): The tilt angle θ as functions of the signal wavelength and the pump wavelength for crystals with fixed doping ratio, i.e., MgLN [MgO(5 mol%):LiNbO3], ZnLN [ZnO(5 mol%):$LiNbO_3$], and InZnLN [In_2O_3(5 mol%):ZnO(5.5 mol%):$LiNbO_3$]. (d-f): The corresponding poling period. In these figures, the signal and the idler photons have the non-degenerated wavelengths under **type-0** phase-matching condition. The solid black line indicates $\theta = 45°$, and the dashed black line indicates $\lambda_s = 2\lambda_p$.

be concluded that the GVM_2 wavelength is the most sensitive one to the temperature increase, i.e., decreases by about 78 nm. In contrast, GVM_1 is not so sensitive, i.e., only increase by 2.8 nm.

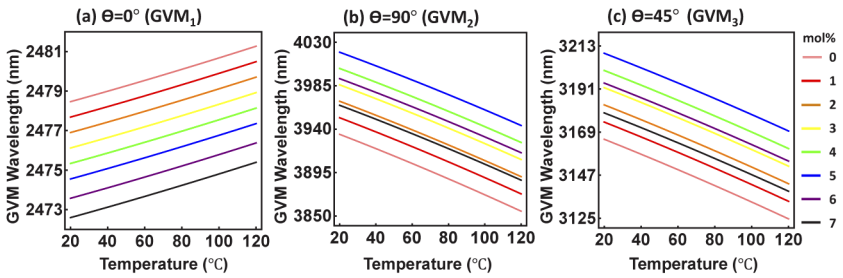

Fig. 5. Three GVM wavelengths of MgLN [MgO(x mol%):LiNbO3] with different doping ratio x (mol%) at different temperatures.

Next, we consider the thermal properties of other doped LN crystals. We compare the case of Mg(5 mol%)LN, Zn(5 mol%)LN, and In(5 mol%)Zn(5.5 mol%)LN in Fig. 6 and Table 2. The most apparent feature in Fig. 6 and Table 2 is that the signal/idler wavelength changes linearly. The wavelength difference between 20 °C and 120 °C, $\Delta\lambda_{GVM}$, is almost the same for three different crystals, i.e., $\Delta\lambda_{GVM1}$, $\Delta\lambda_{GVM2}$, and $\Delta\lambda_{GVM3}$ are about 2.8 nm, 78 nm, and 40 nm, respectively. This phenomenon implies that the thermal-related GVM wavelength is not dominated by the doped elements, but by the main component, $LiNbO_3$. The calculated the poling period of the three crystals at 20 °C are in the range of 14-15 μm, which can be

Optics EXPRESS

realized with the current technology. Note that the thermal expansion of the LN crystals are not considered in the calculation, since such data are not available in the references.

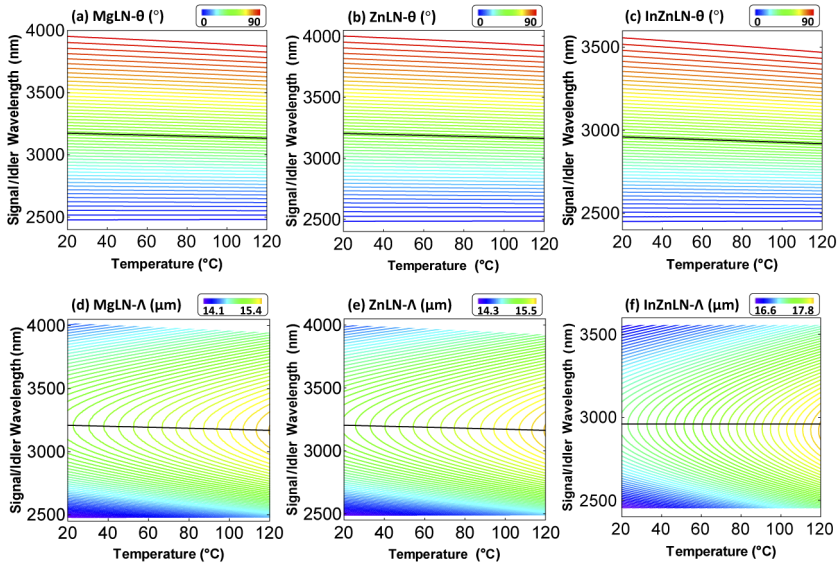

Fig. 6. (a-c): The tilt angle θ as functions of signal (idler) wavelength and temperature for crystals with fixed doping ratio, i.e., MgLN [MgO(5 mol%):LiNbO3], ZnLN [ZnO(5 mol%):$LiNbO_3$], and InZnLN [In_2O_3(5 mol%):ZnO(5.5 mol%):$LiNbO_3$]. (d-f): The corresponding poling period. In these figures, the signal and the idler photons have the degenerated wavelengths under **type-II** phase-matching condition. The solid black line indicates $\theta = 45°$, and the dashed black line indicates $\lambda_s = 2\lambda_p$.

Table 2. Comparison of the GVM wavelengths $\lambda_{GVM1(2,3)}$ at 20 °C, the wavelength difference $\Delta\lambda_{GVM1(2,3)}$ between 20 °C and 120 °C, and the poling period $\Lambda_{GVM1(2,3)}$ under three GVM conditions for three doped LN crystals: Mg(5 mol%)LN, Zn(5 mol%)LN and In(5 mol%)Zn(5.5 mol%)LN.

Crystal Name	MgLN	ZnLN	InZnLN
λ_{GVM1} at 20 °C (nm)	2474.6	2483.7	2450.7
$\Delta\lambda_{GVM1}$ 20-120 °C (nm)	-2.8	-2.8	-2.8
λ_{GVM2} at 20 °C (nm)	4019.7	4002.5	3557.3
$\Delta\lambda_{GVM2}$ 20-120 °C (nm)	75.9	78.1	87.3
λ_{GVM3} at 20 °C (nm)	3209.3	3203.8	2960.2
$\Delta\lambda_{GVM3}$ 20-120 °C (nm)	39.7	40.5	41.1
Λ_{GVM1} at 20 °C (μm)	14.1	14.2	16.6
Λ_{GVM2} at 20 °C (μm)	14.4	14.5	16.7
Λ_{GVM3} at 20 °C (μm)	15.0	15.1	17.2
References	[43]	[44]	[45]

3.4. *Hong-Ou-Mandel interference*

In this subsection, we consider the possible future applications of the spectrally-uncorrelated biphotons in Hong-Ou-Mandel interference [48,49], which is the foundation for many QIP applications such as quantum computation [19], boson sampling [20], and quantum teleportation

Optics EXPRESS

[21]. Figure 7 shows the JSA of the biphotons generated from 5 mol% MgO doped PPLN under GVM_1, GVM_2, and GVM_3 conditions. The spectral ranges for Figs. 7(a-c) are 60 nm, 130 nm, and 40 nm, respectively. The dimension of each JSA matrix is 200×200. Note the photon bandwidths shown in Fig. 7 are just examples. In fact, the bandwidth is strongly dependent on the pulse duration and the crystal length, and the same photon purity can be achieved at different combinations of pump pulse and crystal length.

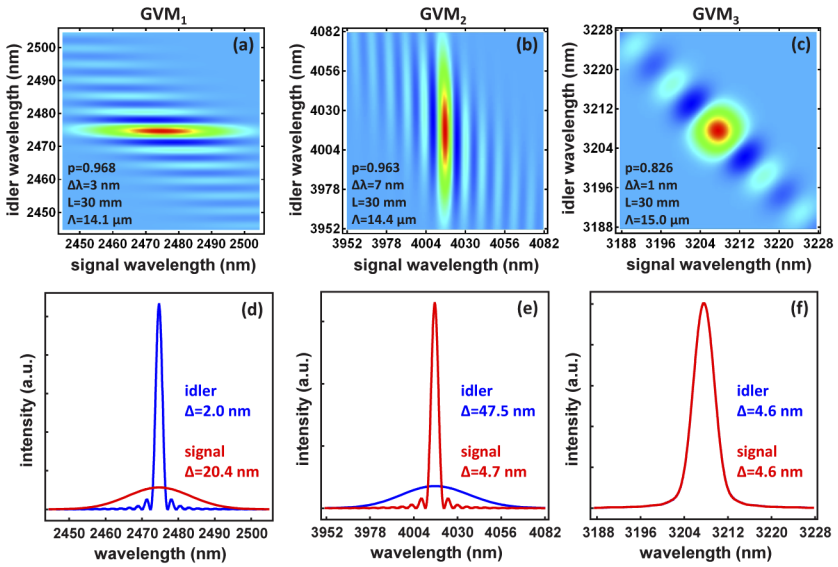

Fig. 7. The JSA and spectra of biphotons generated from 5 mol% MgO doped PPLN under GVM_1, GVM_2, and GVM_3 conditions. The purity p, the pump bandwidth $\Delta\lambda$, the crystal length L, the poling period Λ, and FWHM values (Δ) are listed in the figure. Note the blue curve and red curve are overlapped in (f).

The biphotons under GVM_1 and GVM_2 conditions (see Fig. 7(a, b)) can be used for HOM interference between two independent sources, with a typical experimental setup shown in Refs. [14,50]. In the experiment, two signals s_1 and s_2 are sent to a beamsplitter for interference and then detected by two single-photon detectors, while two idlers i_1 and i_2 are directly sent to single-photon detectors for heralding the signals. The four-fold coincidence probability P_4 as a function of the delay time τ can be described by [14,51,52]

$$P_4(\tau) = \frac{1}{4}\int_0^\infty\int_0^\infty\int_0^\infty\int_0^\infty d\omega_{s_1}d\omega_{s_2}d\omega_{i_1}d\omega_{i_2} \\ |f_1(\omega_{s_1},\omega_{i_1})f_2(\omega_{s_2},\omega_{i_2}) - f_1(\omega_{s_2},\omega_{i_1})f_2(\omega_{s_1},\omega_{i_2})e^{-i(\omega_{s_2}-\omega_{s_1})\tau}|^2, \tag{13}$$

where f_1 and f_2 are the JSAs from the first and the second crystals. Figure 8(a, b) are the simulated HOM interference curves between two heralded signals or two heralded idlers from two independent MgLN sources, with the JSA shown in Fig. 7(a). Without using any narrow bandpass filters, visibility can achieve 96.8%. It can be deduced from Eq.(13) that the visibility, in this case, is determined by the purity (JSA separability) of the heralded signal photons [14].

The bandwidth of the HOM dip depends on the photon bandwidth, which is determined by the crystal length and the pulse duration. If we change the crystal length to be 50 mm, the corresponding HOM dips are 0.64 ps for two signals, and 8.4 ps for two idlers.

The biphotons under the GVM_3 condition (see Fig. 7(c)) can be used for HOM interference between the signal and the idler photons from the same SPDC source, with a typical setup shown

Optics EXPRESS

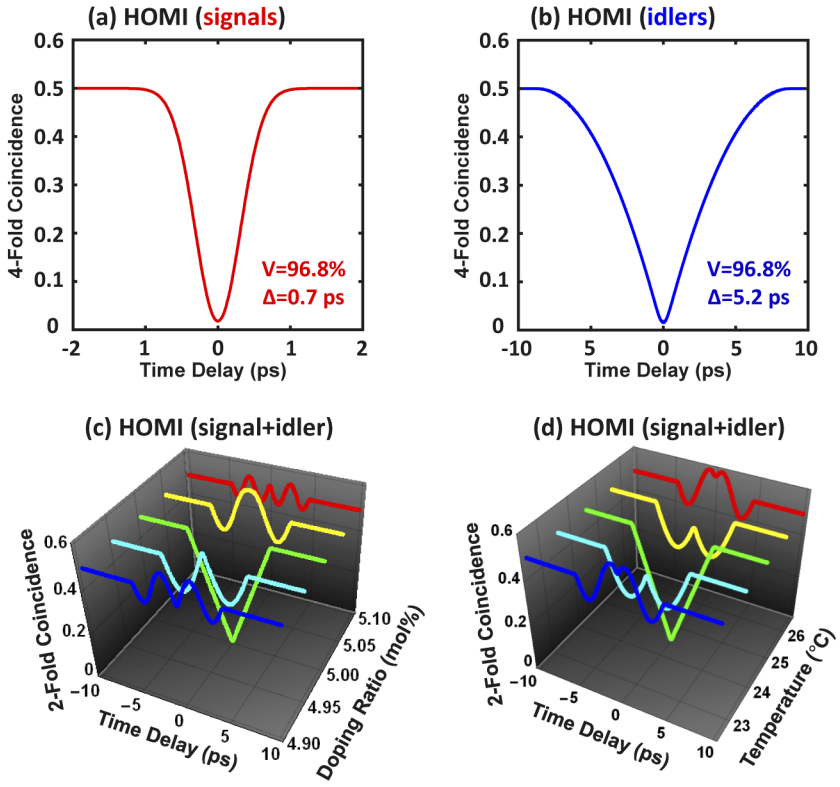

Fig. 8. (a) and (b) are the HOM interference patterns using two heralded signal or idler photons from two independent PPMgLN crystals, with the JSA shown in Fig. 7(a). (c) and (d) are the HOM interference patterns at different doping ratios and different temperatures, using the signal and idler photons from the same PPMgLN crystal, with the initial JSA shown in Fig. 7(c). The visibility (V) and FWHM of the pattern (Δ) are listed in each figure.

in [13,48]. In the experiment, the signal s and the idler i are sent to a beamsplitter for interference and then detected by two single-photon detectors. The two-fold coincidence probability $P_2(\tau)$ as a function of τ is given by [51–53]:

$$P_2(\tau) = \frac{1}{4}\int_0^\infty \int_0^\infty d\omega_s d\omega_i \left|[f(\omega_s,\omega_i) - f(\omega_i,\omega_s)e^{-i(\omega_s-\omega_i)\tau}]\right|^2. \tag{14}$$

The green curve in Fig. 8(c) is the simulated HOM interference pattern between a signal and an idler from the same Mg(5 mol%)LN crystal at 24.5°C, with the JSA shown in Fig. 8(c). Under this condition, the visibility is as high as 100%. By fixing the poling period and changing the doping ratio to 4.90 mol%, 4.95 mol%, 5.05 mol%, and 5.10 mol%, the interference patterns oscillate, as shown in Fig. 8(c). By changing the temperature to 22.5°C, 23.5°C, 25.5°C and 26.5°C, the interference patterns also oscillate, as shown in Fig. 8(d).

4. Discussions

We notice that LN crystal has several different growing methods, and each method has a different effect on the Sellmeier equations. The MgLN, ZnLN, and InZnLN crystals investigated in the Calculation and Simulation section were grown using the Czochralski technique from a congruent melt (mole ratio Li/Nb ≈ 0.942) [43–45]. As shown in Fig. 1, 0 mol% Zn doped LN (i.e., pure

Optics EXPRESS

LN) has the GVM_1, GVM_2, GVM_3 wavelengths of 2478.6 nm, 3931.4 nm , and 3163.6 nm, respectively. In contrast, the pure LN grown from the stoichiometric melt (mole ratio Li/Nb ≈ 1) [54] has the GVM_1, GVM_2, GVM_3 wavelengths of 2681.0 nm, 4653.6 nm, and 3595.8 nm, respectively. Further, using the Sellmeier equations from Ref. [55], the pure LN grown from the congruent melt (mole ratio Li/Nb ≈ 0.937) has the GVM_1, GVM_2, GVM_3 wavelengths of 2678.5 nm, 4361.7 nm, and 3499.1 nm, respectively. These differences are mainly caused by different growing methods. In addition, the LN crystal can also be doped with other elements, which also affect the Sellmeier equations. For example, NdMgLN crystal (grown by the Czochralski technique from a congruent melt in Ref. [56] has the GVM_1, GVM_2, GVM_3 wavelengths of 2615.3 nm, 4562.5 nm, and 3511.5 nm, respectively. We also investigated ErMgLN and MgTiLN crystal [57,58]. However, they do not satisfy the three kinds of GVM conditions. In this calculation, the maximal doping ratio we considered is 7 mol%. In fact, this ratio can still be improved, and we anticipate the wavelength tunability can be further improved at a larger doping ratio.

In this work, limited by the available Sellmeier equations, we only investigate the LN crystals doped with Mg, Zn, In, and Nd. In the future, it is promising to explore more LN crystals doped with different chemical elements and with different doping ratios. Another promising direction is investigating the spectrally pure single-photon state generation from doped PPLN waveguide [59–61] or doped PPLN film [62], which has the merits of higher nonlinear efficiency, easier for integration and microminiaturization. In Fig. 7, the purities are 0.968, 0.963, and 0.826, respectively, and this purity can be further improved to near 1 using the custom poling technique [63,64].

In the section of Calculation and Simulation, we only show the configuration of $o \rightarrow o + e$ in the type-II phase-matching condition. In fact, we also investigate the configuration of $e \rightarrow o + e$. Although the GVM_2 wavelength under this configuration is in the telecom wavelength, the effective nonlinear coefficient, unfortunately, is zero. The reason is analyzed in detail in the Appendix.

For future applications, spectrally uncorrelated biphotons can be used to prepare pure single-photons and entangled photons which can be applied for sensing, imaging, and communication with a quantum-enhanced performance at MIR region. As shown in the section of Calculation and simulation, all the poling periods of the doped PPLN crystals are above 5 μm, which can be easily fabricated using the off-the-shelf technology. So, the MIR-band single-photon source calculated in the work is ready for fundamental research and industry applications, so as to promote the second quantum revolution.

5. Conclusion

In conclusion, we have theoretically studied the preparation of spectrally uncorrelated biphotons at MIR wavelengths from doped LN crystals, including MgO doped LN, ZnO doped LN, and In_2O_3 doped ZnLN with doping ratio from 0 to 7 mol%. The tilt angle, poling period, thermal properties, and HOM interference of the biphotons are calculated under type-II, type-I, and type-0 phase-matching conditions. For 5 mol% MgO doped LN, the three GVM wavelengths are 2474.7 nm, 4016.6 nm, and 3207.6 nm, and the corresponding purities are 0.968, 0.963, and 0.826, respectively. In the calculation of the thermal properties, we found that thermal-related GVM wavelength is not dominated by the doped elements, but by $LiNbO_3$. When the temperature was increased from 20 $^\circ C$ to 120 $^\circ C$, the three GVM wavelengths are increased by about 2.8 nm, -78 nm, and -40 nm, respectively. In the simulation of HOM interference using the 5 mol% MgO doped PPLN, visibility of 96.8% was achieved in a HOM interference between two independent sources, and visibility of 100% was achieved in a HOM interference between the signal and idler from the same SPDC source. The interference patterns oscillate by changing the doping ratio or

Optics EXPRESS

temperature. The spectrally uncorrelated biphotons can be used to prepare pure single-photon source and entangled photon source at MIR wavelengths.

Appendix : The effective nonlinear coefficient

The effective nonlinear coefficient d_{eff} for collinear phase-matching in uniaxial crystals can be deduced as follow [65].

For $o \rightarrow o + e$ phase-matching condition,

$$\begin{aligned} & d_{\text{eff}}(\text{ooe}) = \\ & -d_{xxx}C_\theta C_\phi S_\phi^2 + d_{xyy}C_\theta C_\phi S_\phi^2 - d_{xyz}S_\theta C_\phi S_\phi \\ & +d_{xxz}S_\theta S_\phi^2 + d_{xxy}(C_\theta C_\phi^2 S_\phi - C_\theta S_\phi^3) \\ & +d_{yxx}C_\theta C_\phi^2 S_\phi - d_{yyy}C_\theta C_\phi^2 S_\phi + d_{yyz}S_\theta C_\phi^2 \\ & -d_{yxz}S_\theta C_\phi S_\phi + d_{yxy}(C_\theta C_\phi S_\phi^2 - C_\theta C_\phi^3). \end{aligned} \tag{15}$$

For $e \rightarrow o + e$ phase-matching condition,

$$\begin{aligned} & d_{\text{eff}}(\text{eoe}) = \\ & d_{xxx}C_\theta^2 C_\phi^2 S_\phi - d_{xyy}C_\theta^2 C_\phi^2 S_\phi + d_{xyz}C_\theta S_\theta C_\phi^2 \\ & -d_{xxz}C_\theta S_\theta C_\phi S_\phi + d_{xxy}(C_\theta^2 C_\phi S_\phi^2 - C_\theta^2 C_\phi^3) \\ & +d_{yxx}C_\theta^2 C_\phi S_\phi^2 - d_{yyy}C_\theta^2 C_\phi S_\phi^2 + d_{yyz}C_\theta S_\theta C_\phi S_\phi \\ & -d_{yxz}C_\theta S_\theta S_\phi^2 + d_{yxy}(C_\theta^2 S_\phi^3 - C_\theta^2 C_\phi^2 S_\phi) \\ & -d_{zxx}C_\theta S_\theta C_\phi S_\phi + d_{zyy}C_\theta S_\theta C_\phi S_\phi - d_{zyz}S_\theta^2 C_\phi \\ & +d_{zxz}S_\theta^2 S_\phi + d_{zxy}(C_\theta S_\theta C_\phi^2 - C_\theta S_\theta S_\phi^2), \end{aligned} \tag{16}$$

where $S_\theta = \sin(\theta + \rho)$, $C_\theta = \cos(\theta + \rho)$, $S_\phi = \sin\phi$, $C_\phi = \cos\phi$, and ρ is the walk-off angle. θ is the polar angle, ϕ is the azimuth angle, and Z is the optical axis, as defined in Fig. 9(a). For PPLN under $o \rightarrow o + e$ or $e \rightarrow o + e$ phase-matching conditions, $\rho = 0°$, $\theta = 90°$, and $\phi = 90°$, as shown in Fig. 9(b, c). Therefore,

$$d_{\text{eff}}(\text{ooe}) = d_{xxz} \tag{17}$$

and

$$d_{\text{eff}}(\text{eoe}) = d_{zxz}. \tag{18}$$

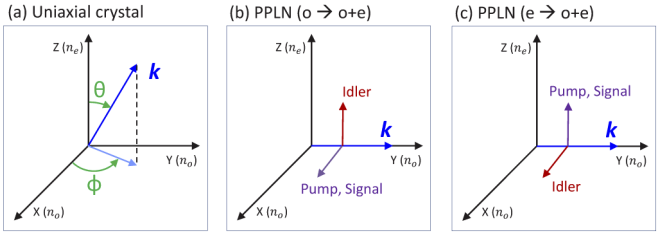

Fig. 9. (a) The general refractive index coordinates for uniaxial crystals. (b, c) The refractive index coordinate for PPLN crystal under ($o \rightarrow o + e$) or ($e \rightarrow o + e$) type-II phase-matching condition.

Optics EXPRESS

The second-order nonlinear coefficient matrix for LN is [66]:

$$d = \begin{pmatrix} 0 & 0 & 0 & 0 & d_{xxz} & d_{xxy} \\ d_{yxx} & d_{yyy} & 0 & d_{yyz} & 0 & 0 \\ d_{zxx} & d_{zyy} & d_{zzz} & 0 & 0 & 0 \end{pmatrix}$$

$$= \begin{pmatrix} 0 & 0 & 0 & 0 & d_{15} & d_{16} \\ d_{21} & d_{22} & 0 & d_{24} & 0 & 0 \\ d_{31} & d_{32} & d_{33} & 0 & 0 & 0 \end{pmatrix} \tag{19}$$

$$= \begin{pmatrix} 0 & 0 & 0 & 0 & -4.6 & -2.2 \\ -2.2 & 2.2 & 0 & -4.6 & 0 & 0 \\ -4.6 & -4.6 & -25.0 & 0 & 0 & 0 \end{pmatrix}.$$

So,

$$d_{\text{eff}}(\text{ooe}) = d_{xxz} = -4.6\,\text{pm/V} \tag{20}$$

and

$$d_{\text{eff}}(\text{eoe}) = d_{zxz} = 0. \tag{21}$$

Therefore, the configuration of $e \rightarrow o + e$ does not exist for PPLN.

Funding. National Key Research and Development Program of China (2018YFA0307400); National Natural Science Foundation of China (11704290, 12074299, 61405030, 61775025, 91836102); the Program of State Key Laboratory of Quantum Optics and Quantum Optics Devices (KF201813).

Acknowledgments. We thank Profs. Zhi-Yuan Zhou, Yan-Xiao Gong, and Ping Xu for helpful discussions.

Disclosures. The authors declare that there are no conflicts of interest related to this article.

References

1. E. Tournie and L. Cerutti, *Mid-infrared optoelectronics materials, devices, and applications* (Woodhead Publishing, 2019).
2. M. Ebrahim-Zadeh and I. T. Sorokina, *Mid-Infrared Coherent Sources and Applications* (Springer Science & Business Media, 2008).
3. R. S. El Shamy, D. Khalil, and M. A. Swillam, "Mid infrared optical gas sensor using plasmonic Mach-Zehnder interferometer," Sci. Rep. **10**(1), 1293–1299 (2020).
4. K. Chen, S. Liu, B. Zhang, Z. Gong, Y. Chen, M. Zhang, H. Deng, M. Guo, F. Ma, and F. Zhu, "Highly sensitive photoacoustic multi-gas analyzer combined with mid-infrared broadband source and near-infrared laser," Opt. Lasers Eng. **124**, 105844 (2020).
5. F. Bellei, A. P. Cartwright, A. N. McCaughan, A. E. Dane, F. Najafi, Q. Zhao, and K. K. Berggren, "Free-space-coupled superconducting nanowire single-photon detectors for infrared optical communications," Opt. Express **24**(4), 3248–3257 (2016).
6. A. Tittl, A.-K. U. Michel, M. Schäferling, X. Yin, B. Gholipour, L. Cui, M. Wuttig, T. Taubner, F. Neubrech, and H. Giessen, "A switchable mid-infrared plasmonic perfect absorber with multispectral thermal imaging capability," Adv. Mater. **27**(31), 4597–4603 (2015).
7. M. Mancinelli, A. Trenti, S. Piccione, G. Fontana, J. S. Dam, P. Tidemand-Lichtenberg, C. Pedersen, and L. Pavesi, "Mid-infrared coincidence measurements on twin photons at room temperature," Nat. Commun. **8**(1), 15184 (2017).
8. R. Soref, "Enabling 2 μm communications," Nat. Photonics **9**(6), 358–359 (2015).
9. K. J. Lee, S. Lee, and H. Shin, "Extended phase-matching properties of periodically poled potassium niobate crystals for mid-infrared polarization-entangled photon-pair generation," Appl. Opt. **55**(34), 9791–9796 (2016).
10. R. A. McCracken, F. Graffitti, and A. Fedrizzi, "Numerical investigation of mid-infrared single-photon generation," J. Opt. Soc. Am. B **35**(12), C38–C48 (2018).
11. L. M. Rosenfeld, D. A. Sulway, G. F. Sinclair, V. Anant, M. G. Thompson, J. G. Rarity, and J. W. Silverstone, "Mid-infrared quantum optics in silicon," arXiv: 1906.10158.

Optics EXPRESS

12. D. Kundys, F. Graffitti, R. A. McCracken, A. Fedrizzi, and B. Kundys, "Numerical study of reconfigurable Mid-IR single photon sources based on functional ferroelectrics," Adv. Quantum Technol. p. 1900092 (2020).
13. S. Prabhakar, T. Shields, A. C. Dada, M. Ebrahim, G. G. Taylor, D. Morozov, K. Erotokritou, S. Miki, M. Yabuno, H. Terai, C. Gawith, M. Kues, L. Caspani, R. H. Hadfield, and M. Clerici, "Two-photon quantum interference and entanglement at 2.1 μm," Sci. Adv. **6**(13), eaay5195 (2020).
14. P. J. Mosley, J. S. Lundeen, B. J. Smith, P. Wasylczyk, A. B. U'Ren, C. Silberhorn, and I. A. Walmsley, "Heralded generation of ultrafast single photons in pure quantum states," Phys. Rev. Lett. **100**(13), 133601 (2008).
15. W. P. Grice, A. B. U'Ren, and I. A. Walmsley, "Eliminating frequency and space-time correlations in multiphoton states," Phys. Rev. A **64**(6), 063815 (2001).
16. A. B. U'Ren, C. Silberhorn, R. Erdmann, K. Banaszek, W. P. Grice, I. A. Walmsley, and M. G. Raymer, "Generation of pure-state single-photon wavepackets by conditional preparation based on spontaneous parametric downconversion," arXiv: quant-ph/0611019 (2006).
17. F. Graffitti, J. Kelly-Massicotte, A. Fedrizzi, and A. M. Branczyk, "Design considerations for high-purity heralded single-photon sources," Phys. Rev. A **98**(5), 053811 (2018).
18. F. Laudenbach, H. Hubel, M. Hentschel, P. Walther, and A. Poppe, "Modelling parametric down-conversion yielding spectrally pure photon pairs," Opt. Express **24**(3), 2712–2727 (2016).
19. I. A. Walmsley and M. G. Raymer, "Toward quantum-information processing with photons," Science **307**(5716), 1733–1734 (2005).
20. M. A. Broome, A. Fedrizzi, S. Rahimi-Keshari, J. Dove, S. Aaronson, T. C. Ralph, and A. G. White, "Photonic boson sampling in a tunable circuit," Science **339**(6121), 794–798 (2013).
21. R. Valivarthi, M. G. Puigibert, Q. Zhou, G. H. Aguilar, V. B. Verma, F. Marsili, M. D. Shaw, S. W. Nam, D. Oblak, and W. Tittel, "Quantum teleportation across a metropolitan fibre network," Nat. Photonics **10**(10), 676–680 (2016).
22. R. Valivarthi, Q. Zhou, C. John, F. Marsili, V. B. Verma, M. D. Shaw, S. W. Nam, D. Oblak, and W. Tittel, "A cost-effective measurement-device-independent quantum key distribution system for quantum networks," Quantum Sci. Technol. **2**(4), 04LT01 (2017).
23. T. Nagata, R. Okamoto, J. L. O'Brien, K. Sasaki, and S. Takeuchi, "Beating the standard quantum limit with four-entangled photons," Science **316**(5825), 726–729 (2007).
24. M. Yabuno, R. Shimizu, Y. Mitsumori, H. Kosaka, and K. Edamatsu, "Four-photon quantum interferometry at a telecom wavelength," Phys. Rev. A **86**(1), 010302 (2012).
25. D. N. Nikogosyan, *Nonlinear optical crystals: a complete survey* (Springer Science & Business Media, 2005).
26. S.-L. Liu, S.-K. Liu, Y.-H. Li, S. Shi, Z.-Y. Zhou, and B.-S. Shi, "Coherent frequency bridge between visible and telecommunications band for vortex light," Opt. Express **25**(20), 24290–24298 (2017).
27. C. Yang, S.-L. Liu, Z.-Y. Zhou, Y. Li, Y.-H. Li, S.-K. Liu, Z.-H. Xu, G.-C. Guo, and B.-S. Shi, "Extra-cavity-enhanced difference-frequency generation at 1.63 μm," J. Opt. Soc. Am. B **37**(5), 1367–1371 (2020).
28. T. Wang, P. Chen, C. Xu, Y. Zhang, D. Wei, X. Hu, G. Zhao, M. Xiao, and S. Zhu, "Periodically poled $LiNbO_3$ crystals from 1D and 2D to 3D," Sci. China Technol. Sci. pp. s11431–019–1503–0 (2020).
29. R.-B. Jin, T. Saito, and R. Shimizu, "Time-frequency duality of biphotons for quantum optical synthesis," Phys. Rev. Appl. **10**(3), 034011 (2018).
30. Y. Kong, F. Bo, W. Wang, D. Zheng, H. Liu, G. Zhang, R. Rupp, and J. Xu, "Recent progress in lithium niobate: Optical damage, defect simulation, and on-chip devices," Adv. Mater. **32**(3), 1806452 (2020).
31. F. Abdi, M. Aillerie, M. Fontana, P. Bourson, T. Volk, B. Maximov, S. Sulyanov, N. Rubinina, and M. Wohlecke, "Influence of Zn doping on electrooptical properties and structure parameters of lithium niobate crystals," Appl. Phys. B **68**(5), 795–799 (1999).
32. G. Zhang, G. Zhang, S. Liu, J. Xu, Q. Sun, and X. Zhang, "The threshold effect of incident light intensity for the photorefractive light-induced scattering in $LiNbO_3$:Fe,M (M=Mg^{2+}, Zn^{2+}, In^{3+}) crystals," J. Appl. Phys. **83**(8), 4392–4396 (1998).
33. M. Palatnikov, I. Biryukova, N. Sidorov, A. Denisov, V. Kalinnikov, P. Smith, and V. Shur, "Growth and concentration dependencies of rare-earth doped lithium niobate single crystals," J. Cryst. Growth **291**(2), 390–397 (2006).
34. S. Dutta, E. A. Goldschmidt, S. Barik, U. Saha, and E. Waks, "Integrated photonic platform for rare-earth ions in thin film lithium niobate," Nano Lett. **20**(1), 741–747 (2020).
35. P. J. Mosley, J. S. Lundeen, B. J. Smith, and I. A. Walmsley, "Conditional preparation of single photons using parametric downconversion: a recipe for purity," New J. Phys. **10**(9), 093011 (2008).
36. R.-B. Jin, R. Shimizu, K. Wakui, H. Benichi, and M. Sasaki, "Widely tunable single photon source with high purity at telecom wavelength," Opt. Express **21**(9), 10659–10666 (2013).
37. K. Edamatsu, R. Shimizu, W. Ueno, R.-B. Jin, F. Kaneda, M. Yabuno, H. Suzuki, S. Nagano, A. Syouji, and K. Suizu, "Photon pair sources with controlled frequency correlation," Prog. Inform. **8**(8), 19–26 (2011).
38. R.-B. Jin, N. Cai, Y. Huang, X.-Y. Hao, S. Wang, F. Li, H.-Z. Song, Q. Zhou, and R. Shimizu, "Theoretical investigation of a spectrally pure-state generation from isomorphs of KDP crystal at near-infrared and telecom wavelengths," Phys. Rev. Appl. **11**(3), 034067 (2019).
39. N. Quesada and A. M. Brańczyk, "Gaussian functions are optimal for waveguided nonlinear-quantum-optical processes," Phys. Rev. A **98**(4), 043813 (2018).
40. R.-B. Jin, W.-H. Cai, C. Ding, F. Mei, G.-W. Deng, R. Shimizu, and Q. Zhou, "Spectrally uncorrelated biphotons generated from "the family of BBO crystal"," Quantum Eng. **2**(2), e38 (2020).

Optics EXPRESS

41. W.-H. Cai, B. Wei, S. Wang, and R.-B. Jin, "Counter-propagating spectrally uncorrelated biphotons at 1550 nm generated from periodically poled MTiOXO$_4$ (M=K, Rb, Cs; X=P, As)," J. Opt. Soc. Am. B **37**(10), 3048–3054 (2020).
42. J.-C. Duan, J.-N. Zhang, Y.-J. Zhu, C.-W. Sun, Y.-C. Liu, P. Xu, Z. Xie, Y.-X. Gong, and S.-N. Zhu, "Generation of narrowband counterpropagating polarization-entangled photon pairs based on thin-film lithium niobate on insulator," J. Opt. Soc. Am. B **37**(7), 2139–2145 (2020).
43. U. Schlarb and K. Betzler, "Influence of the defect structure on the refractive indices of undoped and Mg-doped lithium niobate," Phys. Rev. B **50**(2), 751–757 (1994).
44. U. Schlarb, M. Wöhlecke, B. Gather, A. Reichert, K. Betzler, T. Volk, and N. Rubinina, "Refractive indices of Zn-doped lithium niobate," Opt. Mater. **4**(6), 791–795 (1995).
45. U. Schlarb, B. Matzas, A. Reichert, K. Betzler, M. Wöhlecke, B. Gather, and T. Volk, "Refractive indices of Zn/In-co-doped lithium niobate," Ferroelectrics **185**(1), 269–272 (1996).
46. B. Brecht, D. V. Reddy, C. Silberhorn, and M. G. Raymer, "Photon temporal modes: A complete framework for quantum information science," Phys. Rev. X **5**(4), 041017 (2015).
47. V. Ansari, J. M. Donohue, B. Brecht, and C. Silberhorn, "Tailoring nonlinear processes for quantum optics with pulsed temporal-mode encodings," Optica **5**(5), 534–550 (2018).
48. C. K. Hong, Z. Y. Ou, and L. Mandel, "Measurement of subpicosecond time intervals between two photons by interference," Phys. Rev. Lett. **59**(18), 2044–2046 (1987).
49. A. M. Brańczyk, "Hong-Ou-Mandel Interference," arXiv: 1711.00080 (2017).
50. R.-B. Jin, K. Wakui, R. Shimizu, H. Benichi, S. Miki, T. Yamashita, H. Terai, Z. Wang, M. Fujiwara, and M. Sasaki, "Nonclassical interference between independent intrinsically pure single photons at telecommunication wavelength," Phys. Rev. A **87**(6), 063801 (2013).
51. Z.-Y. J. Ou, *Multi-photon quantum interference* (Springer, 2007).
52. R.-B. Jin, T. Gerrits, M. Fujiwara, R. Wakabayashi, T. Yamashita, S. Miki, H. Terai, R. Shimizu, M. Takeoka, and M. Sasaki, "Spectrally resolved Hong-Ou-Mandel interference between independent photon sources," Opt. Express **23**(22), 28836–28848 (2015).
53. I. A. Grice and W. P. Walmsley, "Spectral information and distinguishability in type-ii down-conversion with a broadband pump," Phys. Rev. A **56**(2), 1627–1634 (1997).
54. M. V. Hobden and J. Warner, "The temperature dependence of the refractive indices of pure lithium niobate," Phys. Lett. **22**(3), 243–244 (1966).
55. D. E. Zelmon, D. L. Small, and D. Jundt, "Infrared corrected Sellmeier coefficients for congruently grown lithium niobate and 5 mol.% magnesium oxide-doped lithium niobate," J. Opt. Soc. Am. B **14**(12), 3319–3322 (1997).
56. G. K. Kitaeva, I. Naumova, A. Mikhailovsky, P. Losevsky, and A. Penin, "Visible and infrared dispersion of the refractive indices in periodically poled and single domain Nd:Mg:LiNbO$_3$ crystals," Appl. Phys. B **66**(2), 201–205 (1998).
57. D.-L. Zhang, Q.-Z. Yang, P.-R. Hua, H.-L. Liu, Y.-M. Cui, L. Sun, Y.-H. Xu, and E. Y.-B. Pun, "Sellmeier equation for doubly Er/Mg-doped congruent LiNbO$_3$ crystals," J. Opt. Soc. Am. B **26**(4), 620–626 (2009).
58. C. Yongmao, W. Jinke, W. Huafu, and L. Bing, "Refractive index measurement and second harmonic generation in a series of LiNbO$_3$: Mg (5 mol%) crystals," Chin. Phys. Lett. **9**(8), 427–430 (1992).
59. X. Cheng, M. C. Sarihan, K.-C. Chang, Y. S. Lee, F. Laudenbach, H. Ye, Z. Yu, and C. W. Wong, "Design of spontaneous parametric down-conversion in integrated hybrid Si$_x$N$_y$-PPLN waveguides," Opt. Express **27**(21), 30773–30787 (2019).
60. C.-W. Sun, S.-H. Wu, J.-C. Duan, J.-W. Zhou, J.-L. Xia, P. Xu, Z. Xie, Y.-X. Gong, and S.-N. Zhu, "Compact polarization-entangled photon-pair source based on a dual-periodically-poled Ti:LiNbO$_3$ waveguide," Opt. Lett. **44**(22), 5598–5601 (2019).
61. Y. Niu, C. Lin, X. Liu, Y. Chen, X. Hu, Y. Zhang, X. Cai, Y.-X. Gong, Z. Xie, and S. Zhu, "Optimizing the efficiency of a periodically poled LNOI waveguide using in situ monitoring of the ferroelectric domains," Appl. Phys. Lett. **116**(10), 101104 (2020).
62. L. Ge, Y. Chen, H. Jiang, G. Li, B. Zhu, Y. Liu, and X. Chen, "Broadband quasi-phase matching in a MgO:PPLN thin film," Photonics Res. **6**(10), 954–958 (2018).
63. A. M. Brańczyk, A. Fedrizzi, T. M. Stace, T. C. Ralph, and A. G. White, "Engineered optical nonlinearity for quantum light sources," Opt. Express **19**(1), 55–65 (2011).
64. C. Cui, R. Arian, S. Guha, N. Peyghambarian, Q. Zhuang, and Z. Zhang, "Wave-function engineering for spectrally uncorrelated biphotons in the telecommunication band based on a machine-learning framework," Phys. Rev. Appl. **12**(3), 034059 (2019).
65. A. Smith, *Crystal nonlinear optics with SNLO examples* (AS-Photonics, 2016).
66. A. Smith, "Snlo," http://www.as-photonics.com/snlo.